Layered Structure Associated with Low Potential Vorticity near the Tropopause Seen in High-Resolution Radiosondes over Japan

KAORU SATO

Arctic Environment Research Center, National Institute of Polar Research, Tokyo, Japan

TIMOTHY J. DUNKERTON

Northwest Research Associates, Bellevue, Washington

(Manuscript received 6 October 2000, in final form 9 April 2002)

ABSTRACT

Horizontal wind and temperature data obtained from operational radiosondes over Japan have recently been available with high vertical resolution. Analyzing these data over 4 yr has indicated horizontal velocity layers with vertical scales of about 5 km lasting for a week or more. The layers appear frequently in winter at several stations simultaneously and are dominant in the height range of 8–16 km. An empirical orthogonal function (EOF) analysis for the time series of layered disturbance amplitude in winter indicates that there are two dominant principal components. The first component (EOF1) describes layered disturbances in the middle of Japan (30°–37°N) and the second one (EOF2) describes disturbances in the south of Japan (23°–30°N). Using global analysis data, the background field of the layered disturbances was examined. An interesting result is that the background potential vorticity (PV) is approximately zero or negative for EOF2 disturbances even though located in a relatively high-latitude region. This fact suggests that the EOF2 disturbances are due to inertial instability. It is also shown that negative PV occurs more than 30% of the time in winter, in a zonally elongated region of 23°–29°N in the western Pacific, on an isentropic surface of 345 K (~10 km altitude). Such a high frequency of negative PV is not observed at other longitudes in this latitude band. To determine the origin of the anomalous PV, backward trajectories were analyzed. For EOF2 disturbances, air parcels having mostly negative PV are traced back to the equatorial region in the longitude band 20°W–140°E within a few days. This is due to a strong northward branch of the Hadley circulation associated with deep convection over the Maritime Continent and a strong northeastward subtropical jet stream. On the other hand, the background PV is low but scarcely negative for EOF1 disturbances. Air parcels at EOF1 stations are traced back to the far west because they are advected mostly by a strong eastward jet stream. Thus, it is inferred that the EOF1 disturbances may be due to inertia–gravity waves trapped in a duct of the westerly jet core.

1. Introduction

Radiosonde observations of temperature and horizontal winds have been made operationally at many stations over the world for several decades mainly for the purpose of numerical weather prediction. These observations, however, are also valuable for research purposes and for topics lying outside the scope of large-scale meteorology. Since radiosonde data sample a single location and have high vertical resolution of $O(100\ \text{m})$ in the troposphere and lower stratosphere, it is possible to analyze various characteristics of small-scale atmospheric disturbances such as gravity waves and equatorial waves.

Small-scale atmospheric phenomena can be examined also by recently developed observational tools with advantages that radiosonde observations do not have. For example, mesosphere, stratosphere, and troposphere (MST) radars (VHF/UHF clear-air Doppler radars), and lidars provide vertical profiles of three-dimensional winds and temperature with fine temporal resolution of a few minutes, in contrast to the 1.5 h typically required for a radiosonde to traverse from the ground to the lower stratosphere. Satellites using occultation techniques provide vertical profiles of temperature globally over any surface, while radiosonde observations are restricted mainly to land areas and ocean islands.

Radiosonde observations nevertheless have significant merits compared with these recently developed observational techniques. The first one is their economical cost. It is easy to make special campaign, as well as operational, observations simultaneously at widely separated stations (Tsuda et al. 1994; Wada et al. 1999) which is difficult for radar and lidar observations. The second merit is spatial resolution. Radiosondes provide in situ data at a single location, while satellite occultation data have a horizontal resolution of several hundred kilometers, which is often insufficient to detect small-scale phenomena. The third advantage is the ac-

Corresponding author address: Dr. Kaoru Sato, Arctic Environment Research Center, National Institute of Polar Research, Kaga 1-9-10, Itabashi, Tokyo 173-8515, Japan.
E-mail: kaoru@nipr.ac.jp

cumulation of operational radiosonde data over many decades. Long-term variability and statistical characteristics of smaller-scale disturbances can be investigated using radiosonde data in various latitude bands (Kitamura and Hirota 1989; Dunkerton 1993b; Dunkerton and Baldwin 1995; Allen and Vincent 1995; Yoshiki and Sato 2000).

So far, small vertical-scale fluctuations observed in radiosonde data have been analyzed mainly in terms of gravity waves or equatorially trapped waves. However, it is sometimes necessary to consider inertial instability as an alternative explanation of small-scale disturbances, particularly in the equatorial region. Inertial instability occurs when the balance of centrifugal force and meridional pressure gradient force is broken for meridional displacements. A criterion for inertial instability is negative (positive) Ertel's potential vorticity in the Northern (Southern) Hemisphere. It is shown theoretically that the mode with the largest growth rate has infinitely large vertical wavenumber for a zonally symmetric background field (Dunkerton 1981), although the vertical wavelength of the most unstable mode can be modified if atmospheric viscosity and/or zonal asymmetry of the field are taken into account (Dunkerton 1983, 1993a; Stevens and Ciesielski 1986; Clark and Haynes 1996).

Hitchman et al. (1987) found ''pancake structures'' in temperature data with high vertical resolution of 2 km acquired by the Limb Infrared Monitor of the Stratosphere (LIMS) instrument in the upper stratosphere and lower mesosphere, and interpreted these features as inertial instability. Usually inertially unstable air is confined to low-latitude regions. A meridional overturning circulation is associated with the northward or southward motions due to inertial instability; this circulation is sometimes referred to as the inertial circulation. Temperature anomalies of opposite sign are caused by upward and downward branches of the inertial circulation at the latitudinal boundaries of unstable cells as detected in Cryogenic Limb Array Etalon Spectrometer (CLAES) data from the *Upper Atmosphere Research Satellite* (*UARS*) by Hayashi et al. (1998). The inertial circulations inferred by Hayashi and Shiotani were confined to a band of longitudes where anomalous potential vorticity (PV) was drawn poleward by a planetary Rossby wave entering the Tropics. O'Sullivan and Hitchman (1992) also demonstrated in a numerical model the importance of local inertial instability in a Rossby wave-breaking event.

There have been only a limited number of observational reports describing inertial instability at relatively high latitudes or at lower altitudes in the upper troposphere and lower stratosphere. Ciesielski et al. (1989) showed cloud wavelets in a region of negative potential vorticity over the south part of the United States using *Geostationary Operational Environmental Satellite* (*GOES*) *West* infrared satellite pictures. The life cycle of the wavelets was approximately 4–5 h and the horizontal wavelength approximately 400 km. They suggested that negative potential vorticity can be generated by radiative heating gradients associated with cirrus clouds.

In this study, we examine operational radiosonde data with high vertical resolution at 18 Japanese stations over a 4 yr period and show the existence of long-lasting layered disturbances in horizontal wind, which appear frequently in winter at several stations simultaneously. Through analysis of PV and back trajectories it is shown that the layered disturbances can be interpreted as, or related to, inertial instability. From their timescale and horizontal extent, we consider that the layered disturbances reported in this study are different from those shown by Ciesielski et al. (1989), although the latitude and altitude of observation are similar. The data are described in section 2 and the existence of layered disturbances is shown in section 3. An empirical orthogonal function (EOF) analysis is made in section 4 to elucidate the large-scale organization and temporal variation of the disturbances. Also, the background field is examined using National Centers for Environmental Prediction (NCEP) reanalysis data. Backward trajectories are calculated in section 5 to determine the origin of the air in which the layered disturbances are embedded. The results are discussed in section 6, and summary and concluding remarks are made in section 7.

2. Data description

The Japan Meteorological Agency (JMA) has archived data from operational radiosonde observations at small vertical sampling intervals since 1995. The vertical intervals of JMA data are about 200 m for temperature and on average about 300 m for horizontal winds, which are finer than those of the World Meteorological Organization (WMO) criteria for the purpose of numerical weather prediction. The accuracy of temperature measurements is 0.1 K. Horizontal winds are estimated as time derivatives of the horizontal position of radiosondes. Time intervals of 1, 2, and 4 min are used to obtain the time derivatives for the height regions roughly corresponding to $z = 0.3$–4.5 km, $z = 4.8$–15 km, and $z > 15.3$ km, respectively. These time intervals are equivalent to about 300-, 600-, and 1.2-km height intervals. Since the horizontal positions of radiosondes are estimated from the temporal variation of elevation and azimuthal angle of the radiosondes, the wind accuracy is not constant and depends on the accuracy of these measured parameters. Wind accuracy is considered to be better than a few meters per second for the radial direction and better than 1 m s^{-1} for the tangential direction in normal atmospheric conditions (Japan Meteorological Agency 1995). Note, in this paper we examine mainly meridional wind fluctuations that are approximately in the tangential direction of winds.

We used twice daily (0000 and 1200 UTC) radiosonde data at 18 stations for 4 yr from 1995 through 1998. The station locations are shown in Fig. 1 and

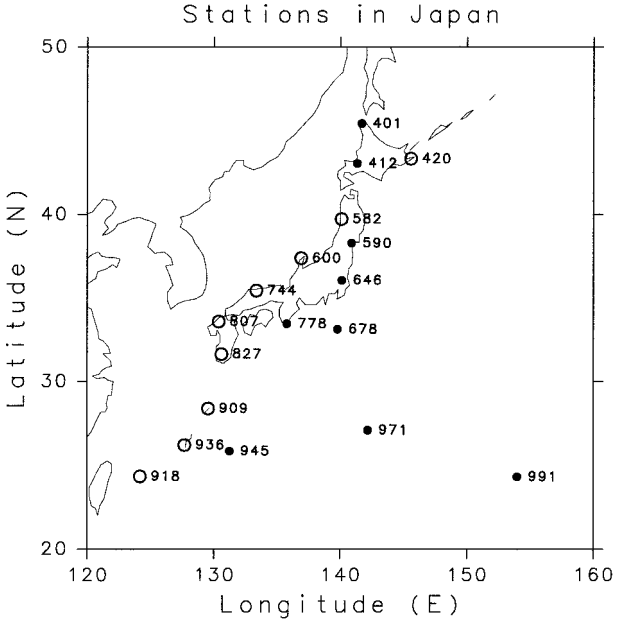

FIG. 1. Radiosonde stations operated by the Japan Meteorological Agency. Numerals on the map show last three digits of the station numbers. Data at stations denoted by open circles are used to make meridional cross sections in this paper.

TABLE 1. List of operational radiosonde stations of the Japan Meteorological Agency.

Station name	Station no.	Latitude	Longitude
Wakkanai	47401	45.4°N	141.7°E
Sapporo	47412	43.1°N	141.3°E
Nemuro	47420	43.3°N	145.6°E
Akita	47582	39.7°N	140.1°E
Sendai	47590	38.3°N	140.9°E
Wajima	47600	37.4°N	136.9°E
Tateno	47646	36.0°N	140.1°E
Hachijojima	47678	33.1°N	139.8°E
Yonago	47744	36.4°N	133.4°E
Shionomisaki	47778	33.5°N	135.8°E
Fukuoka	47807	33.6°N	130.4°E
Kagoshima	47827	31.6°N	130.6°E
Naze	47909	28.4°N	129.5°E
Ishigakijima	47918	24.3°N	124.2°E
Naha	47936	26.2°N	127.7°E
Minamidaitojima	47945	25.8°N	131.2°E
Chichijima	47971	27.1°N	142.2°E
Minamitorishima	47991	24.3°N	154.0°E

listed in Table 1. To make the analysis easier, we interpolated the data to a uniform vertical interval of 200 m using a cubic spline method in the altitude range 0–30 km.

We also used NCEP reanalysis data of geopotential height, zonal and meridional winds, and temperature for the same time period to examine the background field.

3. Existence of layered disturbances

a. Typical examples

Layered structures are often observed in the meridional wind component v at several stations simultaneously in winter. Figure 2a shows a time–height section of meridional wind at Naha (26.2°N, 127.7°E; station number 47936) in the southern part of Japan over 21 days from 20 December 1995 through 10 January 1996. Dots show the tropopause levels estimated from vertical profiles of radiosonde temperature data. The tropopauses are located at two levels: about 16 km (20–30 December and 3–10 January) and 6 km (30 December to 3 January). This double tropopause structure is related to the existence of a strong westerly jet around 11 km, and the appearance of a lower tropopause corresponds to the southward shift of the westerly jet, as shown later. Note also that this double tropopause structure is not clear in the reanalysis data with coarse vertical grids.

Strong and shallow northward winds are observed below the upper tropopause continuously from 25 December to 10 January. Similar layered structure in meridional wind is observed simultaneously at other stations located at almost the same latitude. Figure 3 shows vertical profiles of (unfiltered) meridional wind at 0000 UTC 27 December 1995 at Ishigakijima (24.3°N, 124.2°E; station number 47918), Naha, Naze (28.4°N, 129.5°E; 47909), Minamidaitojima (25.8°N, 131.2°E; 47945), and Chichijima (27.1°N, 142.2°E; 47971). A northward flow around 13 km is observed at all stations. A southward countercurrent is observed at 10.6 km at Naze and at 13.8 km at Chichijima. Another northward flow is observed at 15 km at Chichijima.

To see this layered structure of meridional wind more clearly, we extracted fluctuations using a bandpass filter in the vertical with cutoff lengths of 1.5 and 6 km, and a low-pass filter in time with a cutoff length of 2 days. Figure 4 shows the response function of these filters. Hereafter, we refer to the filtered meridional velocity component as v'. The time–height section of v' at Naha is shown in Fig. 2b. The layered structure is clear in the height region between the upper and lower tropopause levels, and large positive values of v' greater than 7 m s^{-1} are seen around 13 km. From their large amplitude and layered structure similar to that of Fig. 2a, it is confirmed that the layered disturbances observed in Fig. 2b are not an artifact of the vertical filter.

The time–height sections of v' at Ishigakijima and Chichijima are shown in Figs. 2c and 2d, respectively. It is worth noting that there are some phase differences in the vertical between the stations. Judging from the similarity in disturbance structure and timing of appearance, it is inferred that the layered disturbances observed at these stations are due to the same event.

Another example is observed at more northern stations at latitudes of 33°–37°N. The unfiltered meridional winds at Shionomisaki (33.5°N, 135.8°E; 47778) are shown in the time–height section during the time period of 1–20 February 1997 (Fig. 5a). The tropopauses are again located at two levels of about 16 and 8 km. Os-

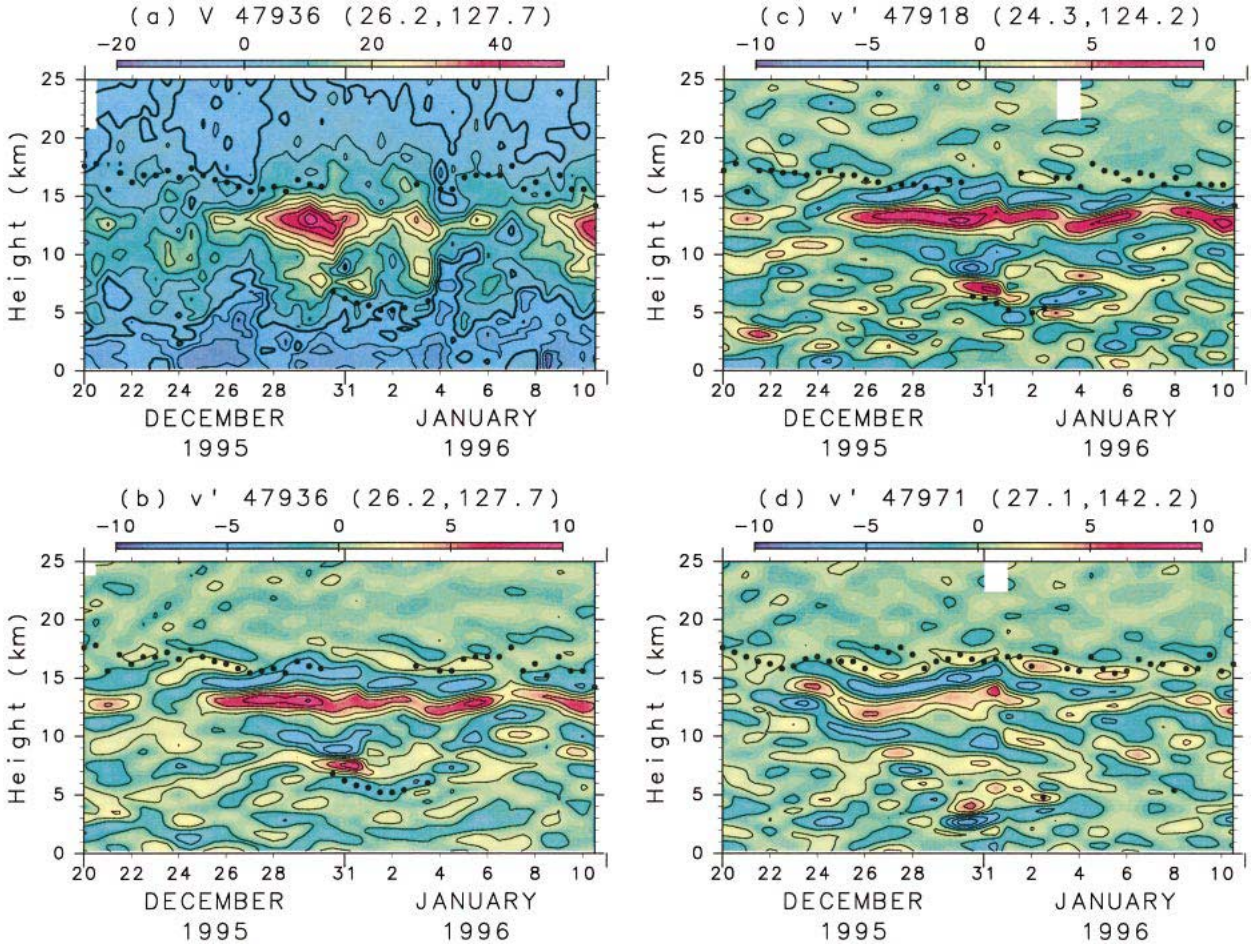

FIG. 2. Time–height sections for the time period of 20 Dec 1995 to 10 Jan 1996 of (a) v at Naha (26.2°N, 127.7°E; station no. 47936), (b) v' at Naha, (c) v' at Ishigakijima (24.3°N, 124.2°E; 47918), and (d) v' at Chichijima (27.1°N, 142.2°E; 47971). Contour intervals are 5 m s^{-1} (. . ., −10, −5, 0, 5, 10, . . .) for (a), and 2 m s^{-1} (. . ., −5, −3, −1, 1, 3, . . .) for (b), (c), and (d). Thick contours show 0 m s^{-1} for (a). Dots indicate the tropopause levels.

cillations with periods of 2–6 days extending through the whole troposphere are seen, which are probably due to synoptic-scale baroclinic waves. Oscillations with shorter periods of 1–2 days, which are not very clear in these twice daily data, are also observed. They are due to the medium-scale waves with barotropic structure trapped around a strong potential vorticity gradient at the tropopause (e.g., Sato et al. 1993, 2000).

An interesting feature is that a layered structure is embedded in these oscillations. For example, a negative anomaly is observed around 16 km in the time period of 9–14 February 1997 with positive anomaly below. The timescale is longer than that of baroclinic waves in the troposphere. Typical vertical scales are 3–4 km. Figure 6 shows vertical profiles of unfiltered meridional winds at Fukuoka (33.6°N, 130.4°E; 47807), Shionomisaki, Hachijojima (33.1°N, 139.8°E; 47678), Yonago (36.4°N, 133.4°E; 47744), and Tateno (36.0°N, 140.1°E; 47646). The layered structure is observed at all stations, though it is not very clear at Hachijojima, which is the westernmost station.

Time–height sections of v' component at Shionomisaki, Hachijojima, and Fukuoka are shown in Figs. 5b, 5c, and 5d, respectively. Layered disturbances having similar structure are observed at these three stations. As in the first case, there is a slight difference in the vertical phase and timing of appearance between the three stations.

Similar layered wind disturbances have frequently been observed by the middle- and upper-atmosphere (MU) radar, an MST radar located at Shigaraki (35.0°N, 136.1°E), at a distance of about 150 km to the north of Shionomisaki. From previous studies (e.g., Hirota and Niki 1986; Sato 1994), it was shown that these disturbances are likely due to inertia–gravity waves (IGW).

We examined zonal wind fluctuations (u'), extracted using the same filters. However, the layered structure observed in v' is not very clear in u', although theoretically a coherent structure should be observed in u'

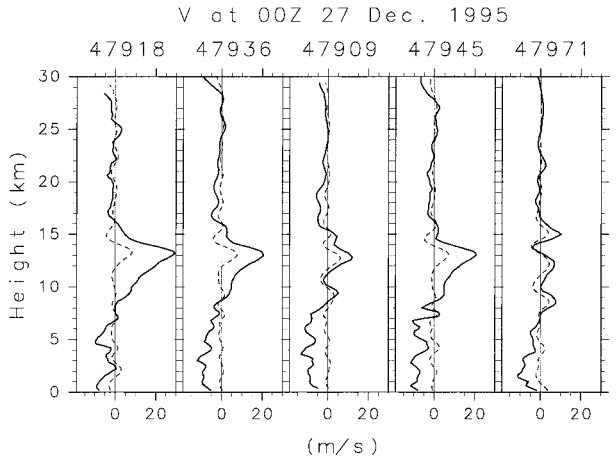

FIG. 3. Unfiltered (solid curves) and filtered (dashed curves) vertical profiles of meridional winds at 0000 UTC 27 Dec 1995 at Ishigakijima (24.3°N, 124.2°E; 47918), Naha (26.2°N, 127.7°E; 47936), Naze (28.4°N, 129.5°E; 47909), Minamidaitojima (25.8°N, 131.2°E; 47945), and Chichijima (27.1°N, 142.2°E; 47971).

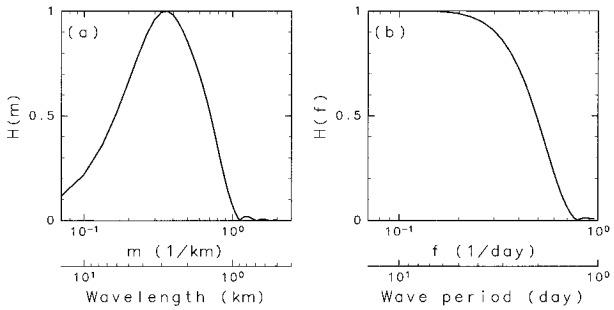

FIG. 4. Response functions of (a) a bandpass filter in the vertical and (b) a low-pass filter in time.

also. The unclear structure in u' may be partly due to contamination of the u' component by the strong westerly jet with its strong vertical shear. Similarly, for the temperature component, it was difficult to distinguish between the layered disturbances and discrete background structure around the tropopause. Thus, the activity of layered disturbances will be examined mainly using v' in the following sections.

b. Mean characteristics

Layered disturbances as in Figs. 2 and 5 are observed mostly in winter when the subtropical westerly jet stream is situated over Japan. Thus, further examination is made for winter periods from 1 December through 10 March in each year. The total number of analyzed vertical profiles is 802 at each station.

To describe the intensity of layered disturbances we calculate an envelope function v_{amp} of v' as a function of height in each profile using a Hilbert transform $\tilde{v}'$ (with phases of all Fourier components shifted by 90°) in z as

$$v_{amp}(z) = |v'(z) + i\tilde{v}'(z)|. \quad (1)$$

Similarly, we define u_{amp} using the u' component.

Figure 7 shows meridional cross sections of zonal (u) and meridional winds (v), u_{amp} and v_{amp} averaged over the four winter periods. The data used are from nine stations denoted by open circles in Fig. 1. Note that the stations chosen here are different from those of Kitamura and Hirota (1989) and cover a wider latitude range with close distribution particularly at lower latitudes.

The axis of westerly jet is located at a latitude of 32°N and altitude of 12 km. A strong northward flow is seen around 13-km altitude. The magnitude of the northward flow is larger at lower latitudes.

The meridional wind amplitudes v_{amp} of the layered disturbances are large to the south of the westerly jet in a height region of 8–16 km. The upper and lower edges of the disturbance region correspond roughly to the tropical and midlatitude tropopauses, respectively.

On the other hand, u_{amp} shows a different distribution from v_{amp}. Zonal wind disturbances are maximized around the westerly jet core, which may be partly due to contamination by the westerly jet itself, as mentioned before. However, the distribution of u_{amp} does not exactly match that of the mean zonal wind. It is obvious that large amplitudes are distributed above and below the jet level at lower latitudes with a shape of "$>$."

A horizontal map of v_{amp} averaged over the four winter periods and for the height range 8–16 km is shown in Fig. 8. The diameter of the circles is proportional to v_{amp} values. A circle located at the bottom right of the figure corresponds to a value of 1 m s^{-1}. There is a tendency for larger amplitudes at lower latitudes in any longitude region.

Contours show the time mean of horizontal wind speed at 200 hPa ($\sim$12 km) based on NCEP reanalysis data. Most stations in Japan are located at the entrance of the westerly jet in a climatological sense.

4. Results of EOF analysis

To examine the simultaneous appearance of layered disturbances at different stations, we calculated correlation coefficients between time series of v_{amp} averaged over the height range 8–16 km at each pair of stations. The results are shown in Table 2, which is sorted by station numbers. The stations with larger station numbers are generally located farther south. Correlation coefficients larger than 0.4 (*40* as shown in Table 2) are italicized. From the table we can see two groups of stations with high correlation: central stations including Wajima (47600), Tateno (47646), Hachijojima (47678), Yonago (47744), Shionomisaki (47778), Fukuoka (47807), and Kagoshima (47827); and southern stations including Naze (47909), Ishigakijima (47918), Naha (47936), Minamidaitojima (47945), and Chichijima (47971). The boundary of the two groups is located around a latitude of 30°N. This regional correlation of

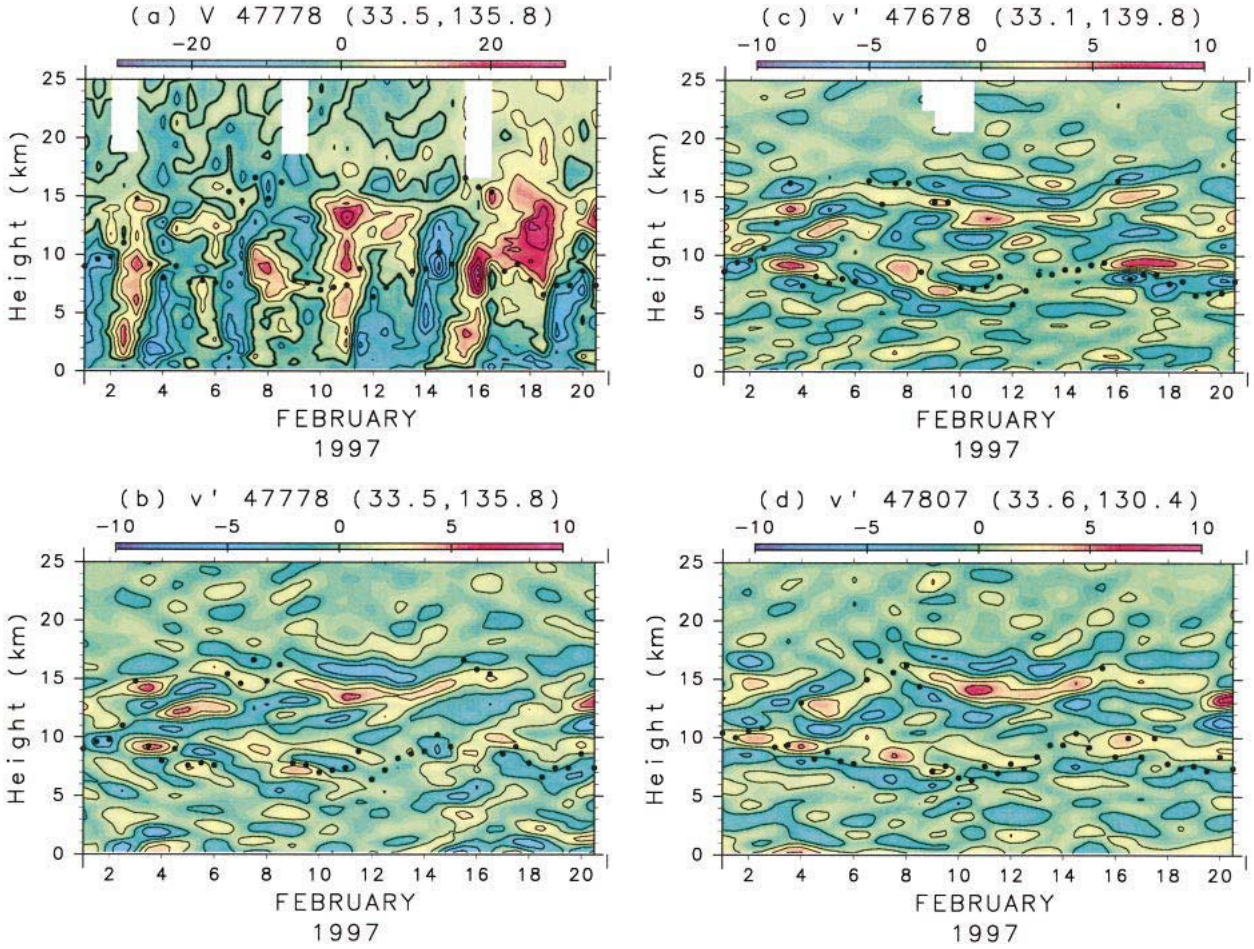

FIG. 5. As in Fig. 2, except for the time period of 1–20 Feb 1997 and stations at (a), (b) Shionomisaki (33.5°N, 135.8°E; 47778), (c) at Hachijojima (33.1°N, 139.8°E; 47678), and (d) Fukuoka (33.6°N, 130.4°E; 47807).

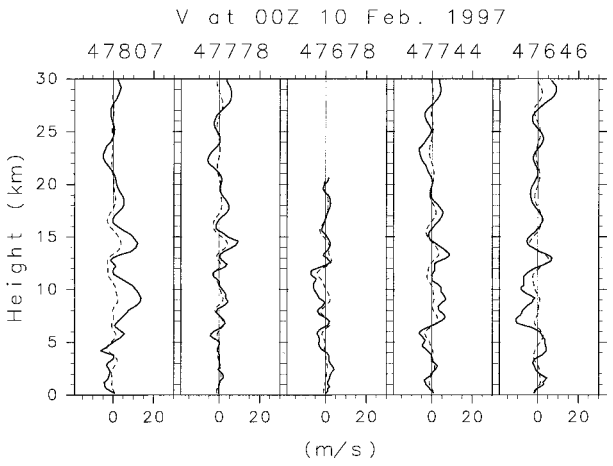

FIG. 6. Unfiltered (solid curves) and filtered (dashed curves) vertical profiles of meridional winds at 0000 UTC 10 Feb 1997 at Fukuoka (33.6°N, 130.4°E; 47807), Shionomisaki (33.5°N, 135.8°E; 47778), Hachijojima (33.1°N, 139.8°E; 47678), Yonago (36.4°N, 133.4°E; 47744), and Tateno (36.0°N, 140.1°E; 47646).

disturbance amplitude can be examined objectively using the EOF method.

a. Two dominant components

For the EOF analysis we excluded the time series at Minamidaitojima (47945) because the data quality is not good in the beginning of 1995. Thus, we used the time series of v_{amp} at the remaining 17 stations. As a result of the EOF analysis, we obtained two dominant modes explaining 25.5% and 20.0% of the total variance, respectively. Patterns of EOF1 and EOF2 components are shown in Figs. 9a and 9b. EOF1 is dominant at central stations, while EOF2 is dominant at southern stations. These patterns are in accord with the two groups indicated by correlation analysis. Thus, hereafter we refer to the central (southern) stations as EOF1 (EOF2) stations.

The time series of EOF1 (EOF2) component and v_{amp} time series at three typical EOF1 (EOF2) stations are shown in Fig. 10 (Fig. 11). Correlation coefficients between v_{amp} time series and each EOF time series are quite high as shown on the right side of each figure.

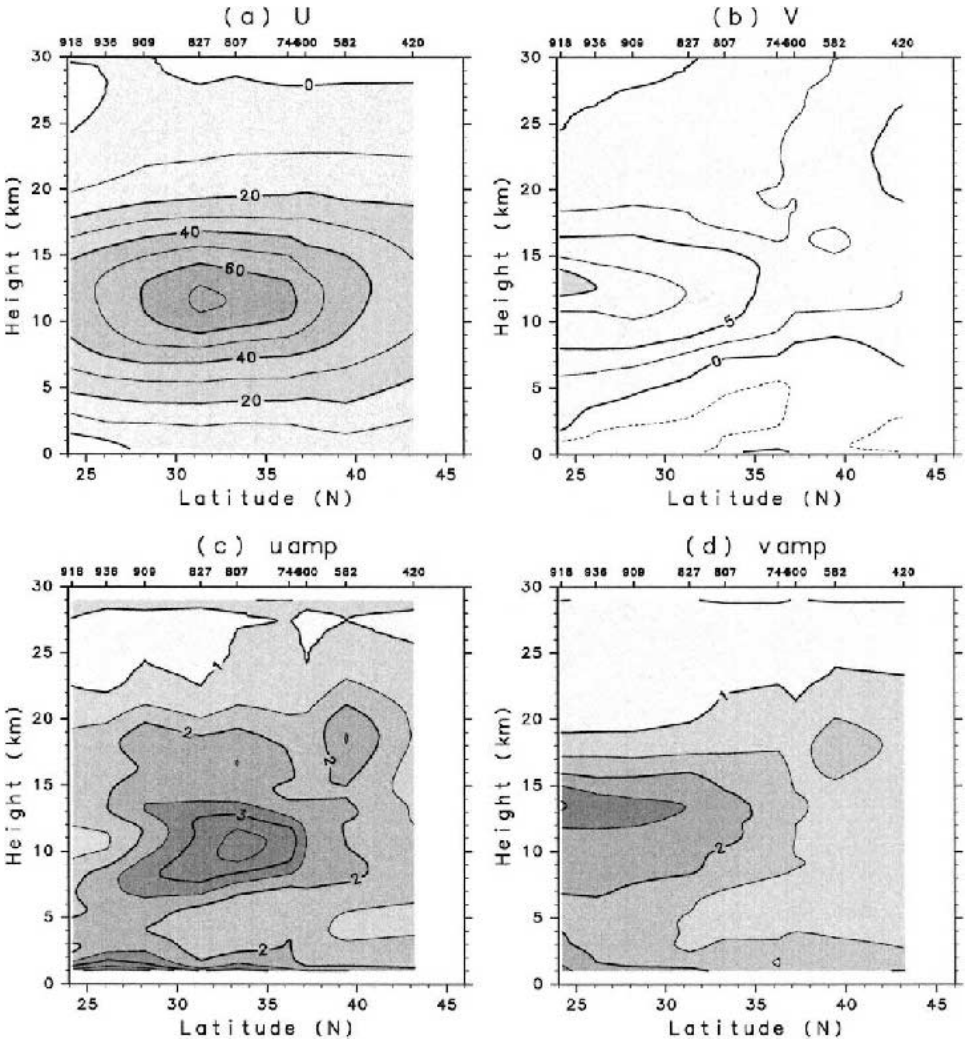

FIG. 7. Meridional cross sections of (a) zonal wind (u), (b) meridional wind (v), (c) zonal (u_{amp}), and (d) meridional (v_{amp}) wind amplitudes of layered disturbances averaged for winter periods in 1995–98. Data at stations denoted by open circles in Fig. 1 are used. Contour intervals are (a) 10 m s^{-1}, (b) 2.5 m s^{-1}, and (c), (d) 0.5 m s^{-1}.

This means that EOF1 and EOF2 modes describe well the appearance of layered disturbances at EOF1 and EOF2 stations, respectively.

The time periods shown in Fig. 2 and in Fig. 5 are denoted by thick lines above EOF1 and EOF2 time series. It is seen that the time periods for Fig. 2 and Fig. 5 are good examples of EOF2 and EOF1 cases, respectively.

In order to see the distribution of disturbance amplitudes for each EOF mode, we calculated the covariance of v_{amp} and EOF time series. The covariance with EOF time series was obtained also for u_{amp}. Figure 12 shows meridional cross sections of the obtained covariance. Large values of v_{amp} are observed at a height of 13 km around 33°N for EOF1 and at a lower latitude of 24°N for EOF2.

On the other hand, u_{amp} distribution is somewhat different. The maximum of u_{amp} values for EOF1 mode is seen around 35°N and large values are distributed upward and downward from the maximum to lower latitudes with a shape of $>$, while the u_{amp} distribution for EOF2 mode is similar to that of v_{amp}.

It should be noted that the patterns of time mean v_{amp} and u_{amp} shown in Fig. 7 are reflected by EOF2 v_{amp} and EOF1 u_{amp} distributions, respectively.

b. Background fields

To determine whether a particular configuration of background fields was favorable for layered disturbances, we made an analysis of u, v, PV, angular momentum, and potential temperature (θ) using NCEP reanalysis data. Spatial derivatives needed for the calculation were obtained using a Fourier transform in the

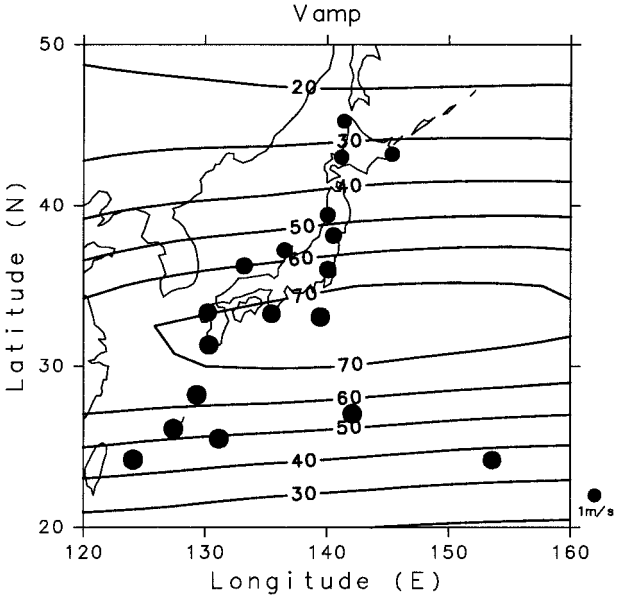

FIG. 8. The amplitude of layered disturbances averaged for a height region of 8–16 km and for winter periods in 1995–98 at each station. The diameter of closed circles is proportional to the disturbance amplitude. A circle at the right-hand bottom corner indicates the amplitude of 1 m s^{-1}. Contours show the time mean horizontal wind speed at 200 hPa at an interval of 10 m s^{-1}.

zonal direction and a cubic spline in the meridional and vertical directions. For convenience, cases with values of EOF1 time series greater (less) than its standard deviation $\sigma_{\mathrm{EOF1}}(-\sigma_{\mathrm{EOF1}})$ are referred to as positive (negative) EOF1 cases. Similarly, positive and negative EOF2 cases are defined. The number of positive (negative) EOF1 case is 128 (123) and that of positive (negative) EOF2 case is 129 (136).

Composite meridional cross sections along a longitude of 135°E are shown in Fig. 13 for positive EOF1 and EOF2 cases. Note that the horizontal axis of Fig. 13 extends to lower latitudes compared with the meridional cross sections made from radiosonde data (Figs. 7 and 12). The latitudinal boundary between EOF1 and EOF2 stations is indicated by a red dashed line. The latitude bands of EOF1 and EOF2 stations are denoted by thick blue lines on the bottom axes of the respective figures.

There are several notable differences between EOF1 and EOF2 composites. The zonal wind jet axis for EOF1 is located slightly more northward than for EOF2 by about 2°. The northward wind at low latitudes is stronger for EOF2 than for EOF1. An interesting and important feature is observed in the PV values. The potential vorticity is small on the lower-latitude (anticyclonic) side of the westerly jet stream. PV values for positive EOF2 cases are significantly smaller compared with those for positive EOF1 cases. The minimum values for positive EOF2 cases are about 0.02 PVU (where PVU is the potential vorticity unit of 10^{-6} m^2 K s^{-1} kg^{-1}). For EOF2 disturbances, v_{amp} is maximized around 25°N at the low-latitude end of the meridional cross section in Fig. 12. Even there, PV values are less than 0.05 PVU, suggesting that the background field for positive EOF2 cases may be occasionally inertially unstable. In fact, the PV values were negative for the typical EOF2 example in Fig. 2 (not shown). On the other hand, PV values for positive EOF1 cases are about 1.6 PVU around 33°N where the v_{amp} maximum is seen for EOF1 disturbances. It is well-known that the PV value of 1.6 PVU corresponds roughly to the tropopause. Thus, the northern half part of EOF1 disturbances is embedded in the stratosphere (see Fig. 12). The potential vorticity is proportional to the meridional gradient of angular momentum along θ surface when the fields vary slowly in longitude. Although real fields are not zonally homogeneous, it is seen that the meridional distance between adjacent contours of angular momentum is large at lower latitudes on an isentropic surface of $\theta = 345$ K around 10 km, where the low PV values are observed. Note that the climatological field is almost zonal (Fig. 8).

Next, we examine the horizontal distribution of low PV on the isentropic surface of $\theta = 345$ K. Figure 14 shows the Montgomery streamfunction M (contours) and PV (shading) averaged for the winter periods. Dark (light) shaded regions have negative (smaller than 0.1 PVU) PV values. The hatched areas are regions with PV values greater than 1.6 PVU corresponding to the stratosphere. An interesting feature is that small PV is observed in the region extending northeastward from south India around 10°N to the western Pacific around 20°N. Although the PV values are not negative as an average, the low values suggest that this region may be inertially unstable occasionally.

It is also worth noting that even for the whole winter average, negative PV values intrude to higher latitudes in the longitudinal region extending from South America to Africa. This suggests that inertial instability may be common there.

To examine the frequency of possible inertial instability, the percentage of time periods with negative PV values was calculated at each grid point on the 345-K surface for the four winter periods. The result is shown in Fig. 15. There is a narrow latitudinal band around 25°N in the western Pacific region where the percentage of negative PV occurrence is greater than 30%. This region corresponds to the locations of EOF2 stations. Therefore it is likely that EOF2 disturbances are due to inertial instability. It is also important to note that the high percentage of negative PV is observed only in this longitude region at such relatively high latitudes. Note that the low PV signature extends across the Pacific all the way to 160°W.

5. Backward trajectory analysis

In order to determine the origin of anomalous PV, we performed a backward trajectory analysis on the isentropic surface of $\theta = 345$ K. The locations of radiosonde

TABLE 2. Correlation between v_{amp} at each pair of stations, which is multiplied by 100. Numerals greater than 40 are italicized.

	Station number (Block designation 47 withheld)																	
	401	412	420	582	590	600	646	678	744	778	807	827	909	918	936	945	971	991
401	*100*	*53*	*47*	31	27	23	15	12	16	8	8	0	−1	2	0	5	−2	−5
412	*53*	*100*	*50*	*43*	34	27	18	14	17	9	7	3	1	9	3	9	−3	2
420	*47*	*50*	*100*	33	26	17	9	2	8	0	1	−2	3	8	7	11	1	1
582	31	*43*	33	*100*	*55*	*43*	30	12	21	15	14	9	7	16	14	15	1	0
590	27	34	26	*55*	*100*	*55*	*42*	21	30	25	25	15	2	12	8	3	0	0
600	23	27	17	*43*	*55*	*100*	*51*	29	*48*	32	36	30	11	8	6	3	−3	−9
646	15	18	9	30	*42*	*51*	*100*	37	*53*	*43*	*42*	28	0	−8	−4	−5	−11	−15
678	12	14	2	12	21	29	37	*100*	34	*65*	*51*	*49*	22	4	6	2	1	−8
744	16	17	8	21	30	*48*	*53*	34	*100*	*51*	*54*	32	0	−12	−4	−7	−11	−5
778	8	9	0	15	25	32	*43*	*65*	*51*	*100*	*63*	*55*	15	−10	−1	−5	−2	−5
807	8	7	1	14	25	36	*42*	*51*	*54*	*63*	*100*	*51*	11	−4	0	−2	−3	−4
827	0	3	−2	9	15	30	28	*49*	32	*55*	*51*	*100*	34	1	10	3	2	−3
909	−1	1	3	7	2	11	0	22	0	15	11	34	*100*	*48*	*63*	*48*	35	11
918	2	9	8	16	12	8	−8	4	−12	−10	−4	1	*48*	*100*	*77*	*69*	39	18
936	0	3	7	14	8	6	−4	6	−4	−1	0	10	*63*	*77*	*100*	*74*	*45*	20
945	5	9	11	15	3	3	−5	2	−7	−5	−2	3	*48*	*69*	*74*	*100*	*56*	18
971	−2	−3	1	1	0	−3	−11	1	−11	−2	−3	2	35	39	*45*	*56*	*100*	33
991	−5	2	1	0	0	−9	−15	−8	−5	−5	−4	−3	11	18	20	18	33	*100*

stations were chosen as initial positions of the trajectories. Six-hourly NCEP reanalysis data in the four winter periods from 1995 through 1998 were used to make integration backward in time over 7 days using a fourth-order Runge–Kutta scheme. The time step was 1 h, which is considered sufficiently small because a shorter time step of 30 min provided almost the same results. A cubic spline method was used for time interpolation. The backward trajectories were calculated for each station beginning every 6 h for the whole winter period. The total number of trajectories is 1464 for each station. We will show typical examples of trajectories for positive EOF1 and EOF2 cases in section 5a. The statistical difference in trajectory distribution between stations for the four winter periods is shown in section 5b. The difference in trajectory statistics between positive and negative EOF cases is examined in section 5c.

a. Case studies

Results of integration starting at 0000 UTC 27 December 1995 and at 0000 UTC 10 February 1997 are shown in Figs. 16 and 17, as typical examples of positive EOF2 and EOF1 cases, respectively. The top figures (a) show backward trajectories for 7 days starting at stations belonging to each EOF category. Dots indicate positions at 0000 UTC every day. The bottom figures (b) show Montgomery streamfunction and PV at the initial time.

For the positive EOF2 case (Fig. 16), it is clear that air parcels at all EOF2 stations are traced back to the equatorial region south of Japan within only a few days. The trajectories are due to advection by northeastward winds which are likely associated with the Hadley circulation over the Maritime Continent. It is also important to note that negative PV values are observed around

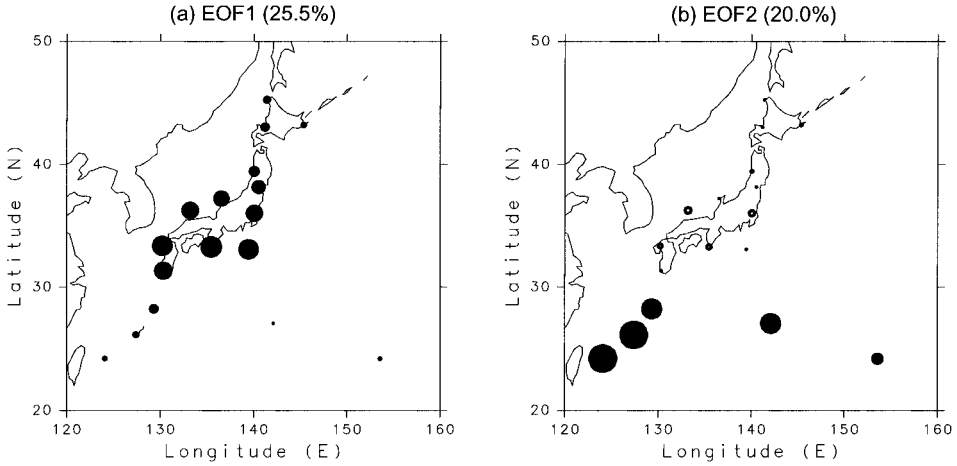

FIG. 9. A pattern of (a) EOF1 and (b) EOF2 components. Positive and negative values are indicated by closed and open circles, respectively. The diameter of the circles is proportional to EOF values.

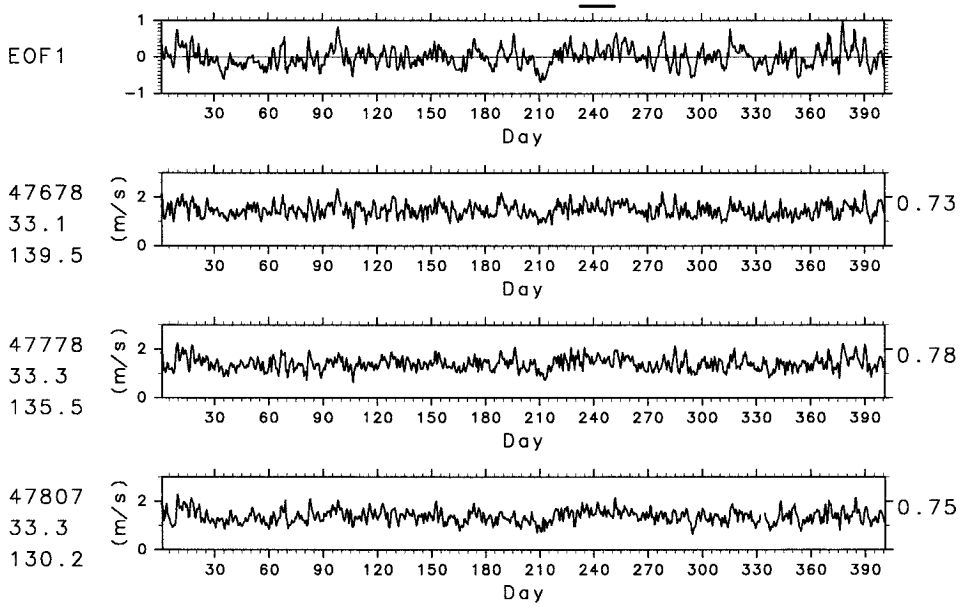

FIG. 10. Time series of the EOF1 component, and v_{amp} at Hachijojima (47678), Shionomisaki (47778), and Fukuoka (47807).

EOF2 stations, suggesting that the layered disturbances are due to the inertial instability.

For the positive EOF1 case (Fig. 17), trajectories starting at EOF1 stations are almost zonal due to the existence of strong westerly jet as seen from the streamfunction. PV values are positive and mostly stratospheric at EOF1 stations. We infer that EOF1 disturbances are not due to in situ inertial instability near Japan since the PV values are not anomalous. However, we speculate that inertial instability may have been important in the initial excitation of EOF1 layered disturbances because air parcels of several southern EOF1 stations originate in the low-latitude region of Africa and the Atlantic Ocean where negative PV values are frequently observed (Fig. 14). The inertial instability contains upward and downward motions at the edge of the anomalous PV region, which would excite IGW. The IGW would survive, perhaps as ducted modes, even after at-

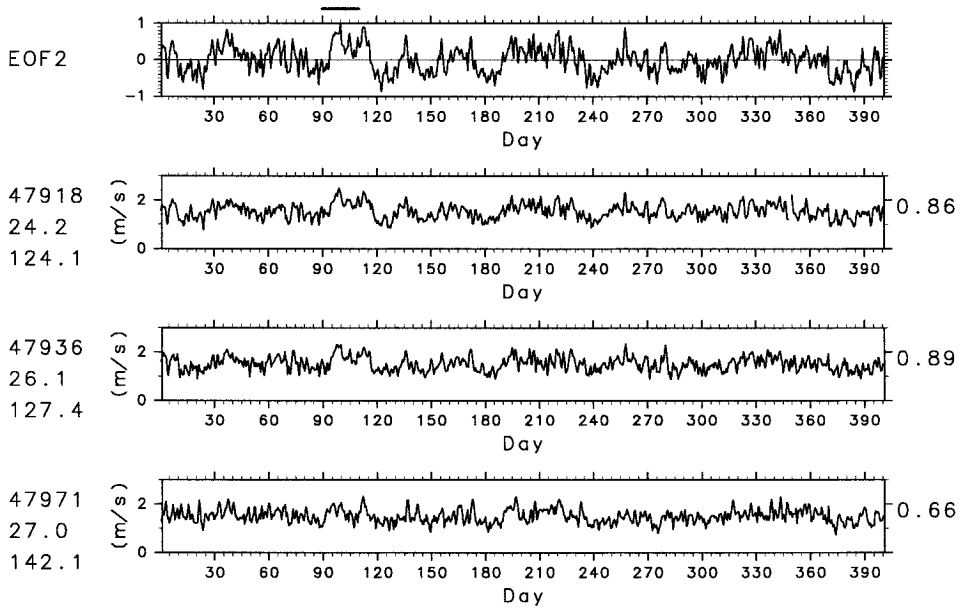

FIG. 11. Time series of the EOF2 component, and v_{amp} at Ishigakijima (47918), Naha (47936), and Chichijima (47971).

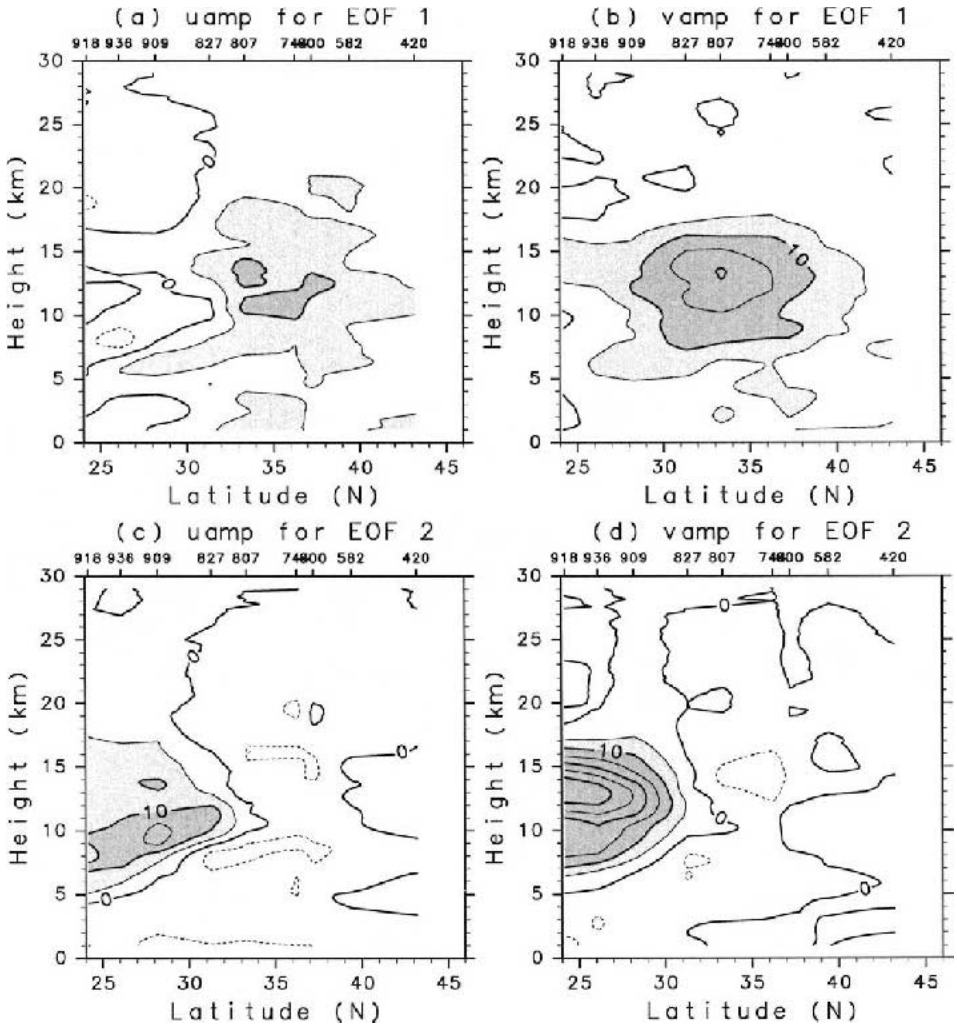

FIG. 12. Meridional cross sections of covariance of (a) u_{amp} and (b) v_{amp} with the EOF1 time series. Results for the EOF2 time series are also shown for (c) u_{amp} and (d) v_{amp}.

mospheric conditions become neutral to inertial instability along their path of propagation.

b. Statistical characteristics

Using all trajectories for the four winter periods starting at each station, the number of trajectories reaching inside the 2.5° × 2.5° rectangle centered at each grid point is calculated for each time lag (Fig. 18). Contours show the same number (10) of trajectories for each radiosonde station. Note that the number 10 does not have meaning by itself because it depends on the grid spacing. Line types of the contours are changed according to the EOF groups: thick contours are for EOF1 stations and thin contours are for EOF2 stations.

It is seen that the trajectories are clearly divided into two groups according to the EOF groups. Air parcels at EOF1 stations are traced back farther to the west. This is likely due to the existence of a strong westerly jet. Air parcels at EOF2 stations have different trajectories from those of EOF1 stations. On day 1, air parcels are distributed in the southwest of Japan; on day 3, the distribution is elongated zonally with slight tilt of the west-northwest direction. On day 5, the distribution is spread more zonally in the equatorial region. On day 7, a large percentage is mostly seen around the equator to the south of Japan. On days 5 and 7, separation of distribution for EOF1 and EOF2 stations is clear. This result suggests that air parcels at EOF1 and EOF2 stations have different origins, consistent with the results of EOF analysis indicating that EOF1 and EOF2 disturbances occur independently.

c. Difference of trajectories between positive and negative EOF cases

Figures 19a and 19b show the distribution of trajectories for positive and negative EOF2 cases on day 3.

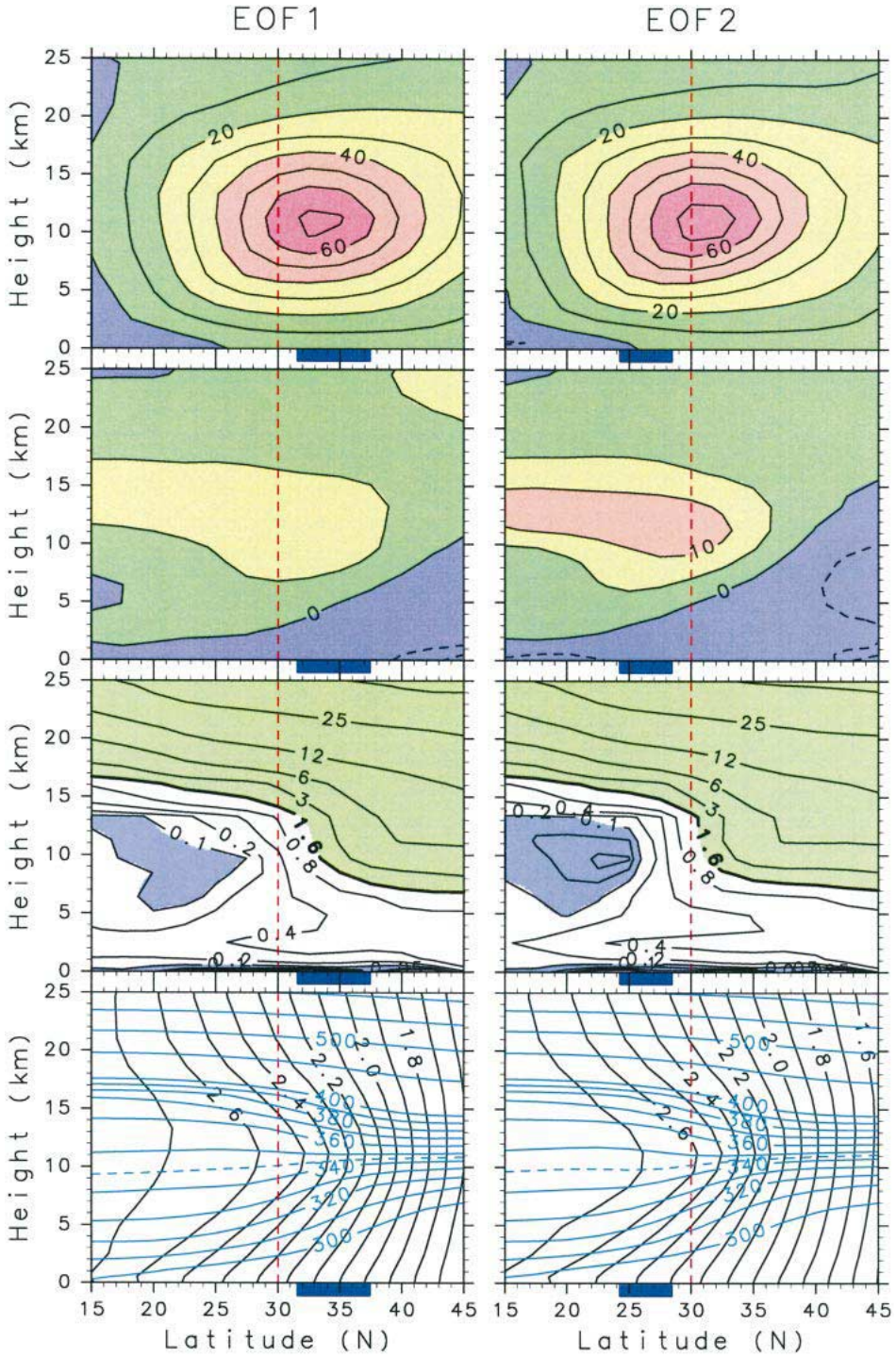

FIG. 13. Composite of meridional cross sections along a longitude of 135°E, from top to bottom, of zonal (u) and meridional (v) winds, potential vorticity (PV), and angular momentum (AM, black contours) with potential temperature (θ, blue contours) for positive EOF1 (left) and positive EOF2 cases (right). Contour intervals are 10 m s^{-1} for u, 5 m s^{-1} for v, and 0.1×10^{-9} m^2 s^{-1} for AM. Units for θ are K. Contour intervals for PV are 0.025, 0.05, 0.1, 0.2, 0.4, 0.8, 1.6, 3, 6, 12, 25, 50, and 100 PVU (PVU $\equiv$ 10^{-6} m^2 K s^{-1} kg^{-1}). The regions with PV values smaller than 0.1 PVU (greater than 1.6 PVU) are colored by blue (green). The latitudinal boundary (30°N) between EOF1 and EOF2 stations is indicated by a red dashed line. The latitude bands of EOF1 and EOF2 stations are denoted by thick blue lines on the bottom axes of the respective figures.

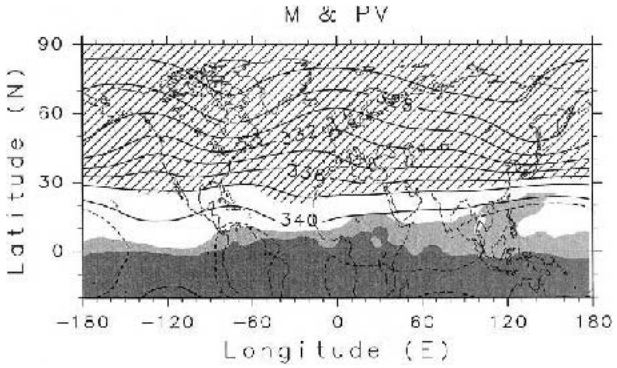

FIG. 14. A contour map of Montgomery streamfunction on the surface of $\theta = 345$ K averaged for winter periods. Contour intervals are 2×10^3 m^2 s^{-2}. Dark (light) shading shows the region where potential vorticity is negative (less than 0.1 PVU). The stratospheric regions (i.e., PV $>$ 1.6 PVU) are hatched.

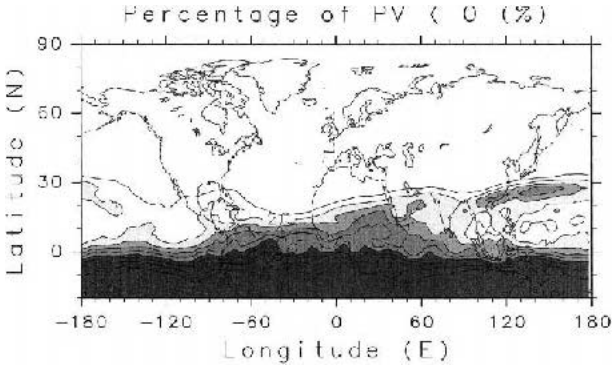

FIG. 15. A contour map of the percentage of times when potential vorticity is negative at each grid point in winter periods on an isentropic surface of 345 K. Contour intervals are 10%. The regions with percentages greater than 20% are shaded. The region with larger percentage is more darkly shaded.

The trajectories of positive EOF2 cases are distributed farther to the south than those of negative EOF2 cases and spread widely to the west. These origins correspond to the regions where anomalous PV is frequently observed: the equatorial region to the south of Japan and over northern Africa at low latitudes (Fig. 15).

The characteristic distribution of trajectories of positive EOF2 cases can be understood by the morphology of the background wind field. Figure 20 shows the correlation between EOF2 time series and background winds. As background winds, we took the horizontal wind speed at 250 hPa to see the relation to the subtropical jet and the meridional wind at 200 hPa to see the relation of the northward branch of Hadley circulation (see Fig. 13).

A clear dipole structure is observed in the correlation map for the horizontal wind speed in East Asia, corresponding to the preference of southward position of the westerly jet (Fig. 13). An interesting feature is that the region with positive correlation is elongated westward and southward. The west end of the correlation contour of 0.3 reaches near the equator around a longitude of 90°W. As for the correlation with meridional wind, high positive correlation is observed to the south of Japan. We made a correlation analysis by taking time lag into account. It was found that a strong subtropical jet slightly shifted to the south and a strong northward flow associated with Hadley circulation precedes the appearance of EOF2 disturbances by 1 day.

The statistics of the trajectories for positive and negative EOF1 cases are shown in Figs. 21a and 21b, respectively. Trajectories of positive EOF1 cases are distributed in more southward regions compared with negative EOF1 cases. It is interesting that some positive EOF1 trajectories originate in the Indian Ocean region, where PV values are frequently negative (Fig. 15). Since PV values at EOF1 stations are mostly positive as seen in Fig. 15, EOF1 disturbances are not due to in situ inertial instability. However, this statistical result also suggests that inertial instability may trigger EOF1 disturbances in the equatorial zone long before they reach Japan.

We made correlation analysis in order to see the morphology of the background field for EOF1 disturbances. In the correlation map for horizontal winds, a dipole structure, but with opposite sign to the EOF2 cases, is observed (not shown). This suggests the preference of a northward position of the westerly jet, in harmony with the results of composite analysis (Fig. 13). However, a meaningful correlation is not observed for the meridional flow.

6. Discussion

Based on the results shown in previous sections, we consider three mechanisms possibly responsible for the layered disturbances: mountain waves, inertial instability, and inertia–gravity waves trapped in the westerly jet. Two characteristic features of the layered disturbances are their long duration and short vertical scale. The phenomena listed above have such characteristics in some circumstances.

a. Mountain waves

Mountain waves are gravity waves excited by strong winds over topography. They generally have almost zero ground-based phase velocity, although modulated by a slowly varying background field (e.g., Sato 1990). Thus the phase structure is almost steady, similar to the layered disturbances. However, it can be shown that there is little possibility of mountain waves in our case.

First, the horizontal group velocity is almost zero for mountain waves, unless strongly nonlinear processes or rapid changes of the background winds are present. This means that mountain waves are local phenomena, contradicting the fact that the layered disturbances appear simultaneously at several stations separated from one another by a few hundred kilometers.

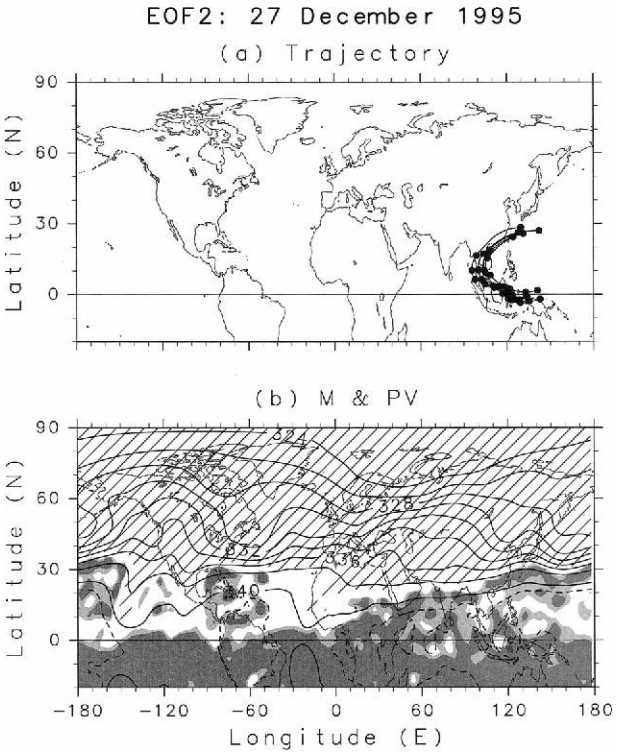

FIG. 16. (a) Backward trajectories starting at EOF2 stations at 0000 UTC 27 Dec 1995. The distance between dots in each trajectory corresponds to 1 day. (b) A contour map of Montgomery streamfunction at 0000 UTC 27 Dec 1995. Contour intervals are 10^3 m^2 s^{-2}. Dashed curves are the contours of 340.5×10^3 m^2 s^{-2}. Dark (light) shaded areas are the regions with negative potential vorticity (smaller than 0.1 PVU). The stratospheric regions (i.e., PV $>$ 1.6 PVU) are hatched.

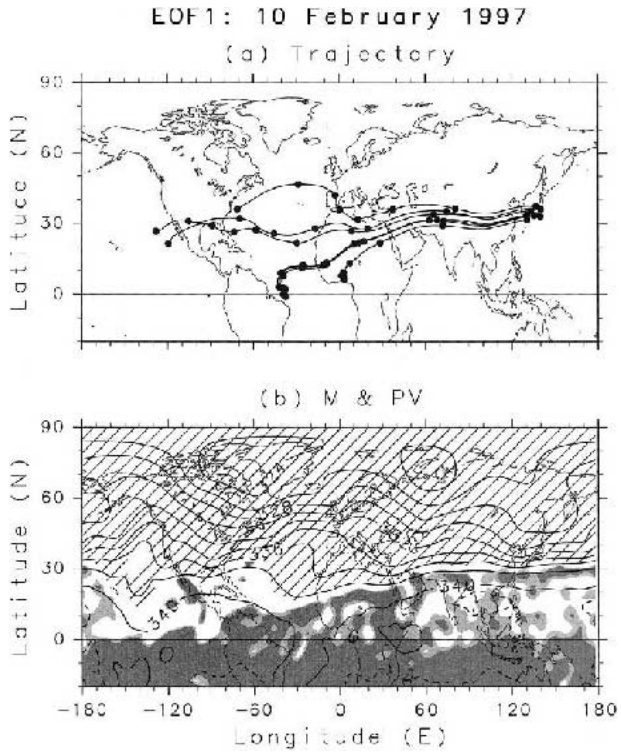

FIG. 17. The same as in Fig. 16, but for the time periods starting at EOF1 stations at 0000 UTC 10 Feb 1997.

Second, it is difficult for stationary mountain waves to have such short vertical wavelengths in a strong westerly jet. The direction of their phase propagation depends on the orientation of the mountains. However, since topography has a three-dimensional structure generally, it is safe to assume that excited mountain waves have intrinsic phase velocities opposite to the background surface wind, that is, westward in the westerly surface wind of winter. The dispersion relation of nonhydrostatic inertia–gravity waves is

$$\hat{c}^2 = \frac{N^2 + f^2 m^2/k^2}{m^2 + k^2} \tag{2}$$

(Gill 1982), where $\hat{c}$ is the phase velocity relative to the background wind (i.e., intrinsic phase velocity), k and m are the horizontal and vertical wavenumber of gravity waves, respectively, and N and f are the buoyancy and inertial frequencies of the background field. Taking 20 h as a typical value of the inertial period in Japan, $\hat{c}$ can be expressed as a function of horizontal wavelength as shown in Fig. 22. We show two typical values of 5 and 10 min for buoyancy periods in the stratosphere and troposphere, respectively (Figs. 22a and 22b), because the height region of 8–16 km, where the layered disturbances are dominant, is sometimes in the stratosphere and sometimes in the troposphere.

From this figure, gravity waves with longer horizontal wavelengths have larger intrinsic phase velocities, while gravity waves with longer vertical wavelengths have larger intrinsic phase velocities. The dispersion curves are flat in the middle because the intrinsic phase velocity is not a function of k for intermediate, that is, hydrostatic and nonrotating, gravity waves.

Westerly winds are greater than 40 m s^{-1} in the height range 8–16 km at longitudes where EOF1 and EOF2 layered disturbances are dominant. Thus, mountain waves should have negative intrinsic phase speeds greater than 40 m s^{-1}. Horizontal wavelengths of gravity waves with $\hat{c} < -40$ m s^{-1} are close to the upper limit for vertical wavelengths shorter than 7 km in both figures. At this limit, the vertical group velocity is close to zero. It is unlikely that such gravity waves would propagate energy upward from the ground to the jet level.

b. Inertial instability

The most promising candidate for EOF2 disturbances is inertial instability. Results of the analysis of the background field and the backward trajectories described in previous sections indicate that air parcels in which EOF2 disturbances are embedded are frequently iner-

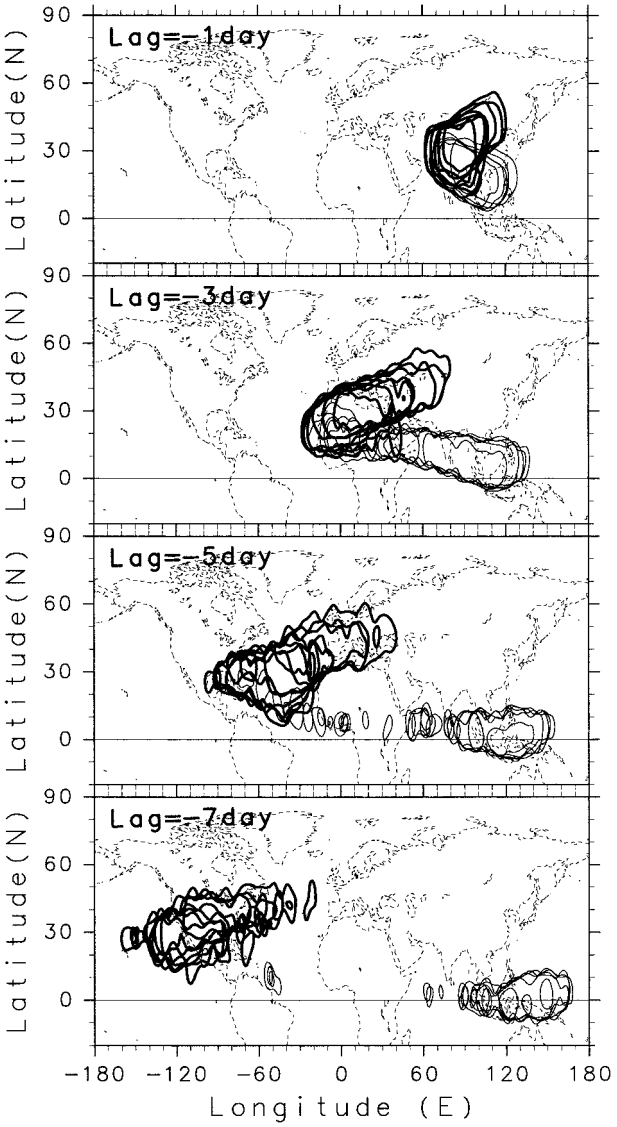

FIG. 18. Horizontal maps of contours indicating the region where the number of backward trajectories is 10, for days 1, 3, 5, and 7 (from top to bottom) starting at EOF1 (thick curves) and EOF2 (thin curves) stations.

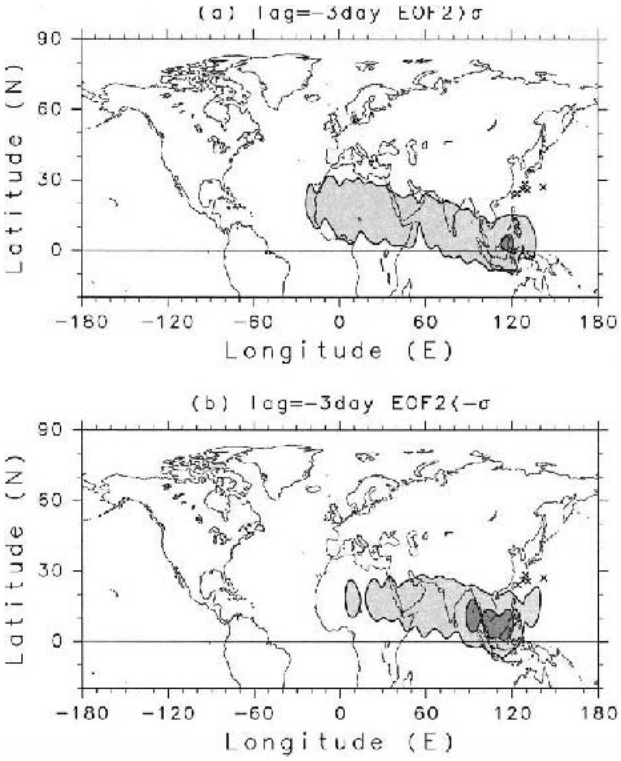

FIG. 19. The same as in Fig. 18, but for all trajectories starting at EOF2 stations. Distribution for (a) positive and (b) negative EOF2 cases. Contours indicate the regions where the numbers of backward trajectories are 5 and 10. The region with a larger number of trajectories is more darkly shaded.

tially unstable. Figure 23 shows the percentage of time periods with negative PV values for positive (top) and negative (bottom) EOF2 cases. Greater percentages spreading more widely are observed to the south of Japan for positive EOF2 cases than for negative EOF2 cases and compared with the climatology (Fig. 15). Moreover, compared with negative EOF2 cases, the percentages for positive EOF2 cases are large in the tropical region of Africa and the Indian Ocean from which some air parcels at EOF2 stations have their origin. This difference also supports the possibility of inertial instability for EOF2 disturbances.

Moreover, EOF2 disturbances have characteristics consistent with inertial instability. The inertial instability is an instability for horizontal displacements in a vortex where angular momentum decreases outward, and mostly for meridional displacements in a zonally rotating atmosphere as in the present case. Thus, large amplitudes of meridional wind components observed for EOF2 disturbances are consistent with the nature of inertial instability.

Another piece of evidence is the covariance of u' and v'. It is theoretically predicted that the covariance of u' and v' components should be negative as follows. For simplicity, we assume a zonal basic flow, which is almost the case for the present field. It is known that such a flow is unstable for the zonally symmetric disturbances when PV < 0 in the Northern Hemisphere. For the modes of inertial instability, a linearized zonal momentum equation becomes

$$\omega_i u' + (\overline{u}_y - f)v' = 0, \tag{3}$$

where ω_i is the growth rate. Since the Richardson number $\mathrm{Ri} \equiv N^2/\overline{u}_z^2$ is much greater than 1 for the present case (not shown in detail), the condition of inertial instability becomes $\overline{u}_y - f > 0$ (Andrews et al. 1987). Thus, the sign of covariance of u' and v' should be negative. Figure 24 shows the composite of the product of u' and v' in the meridional cross section. In the region at latitudes lower than 30°N around a height of 10 km

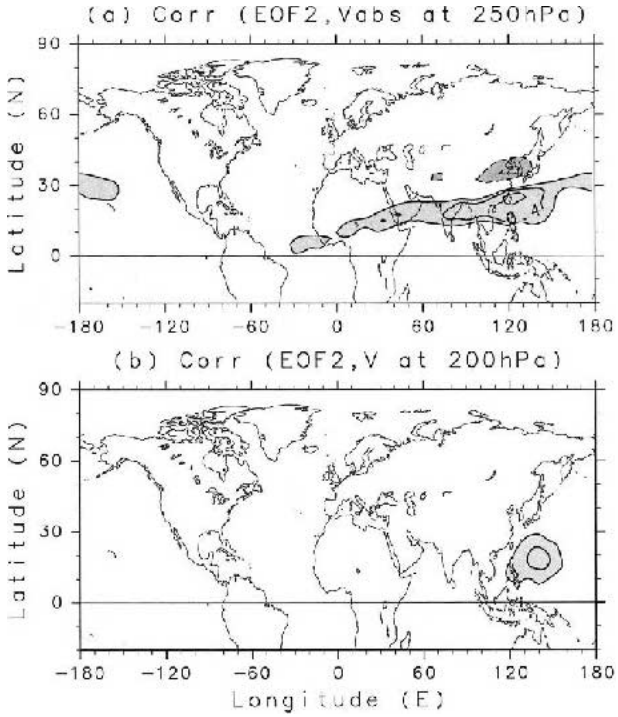

FIG. 20. Horizontal maps of correlation coefficients with EOF2 time series. (a) Correlation of the horizontal wind speed at 250 hPa with EOF2 time series. (b) Correlation of the meridional wind at 200 hPa with EOF2 time series. Solid curves show positive correlation coefficients greater than 0.3 and dashed curves show negative ones less than −0.3. Contour interval is 0.1.

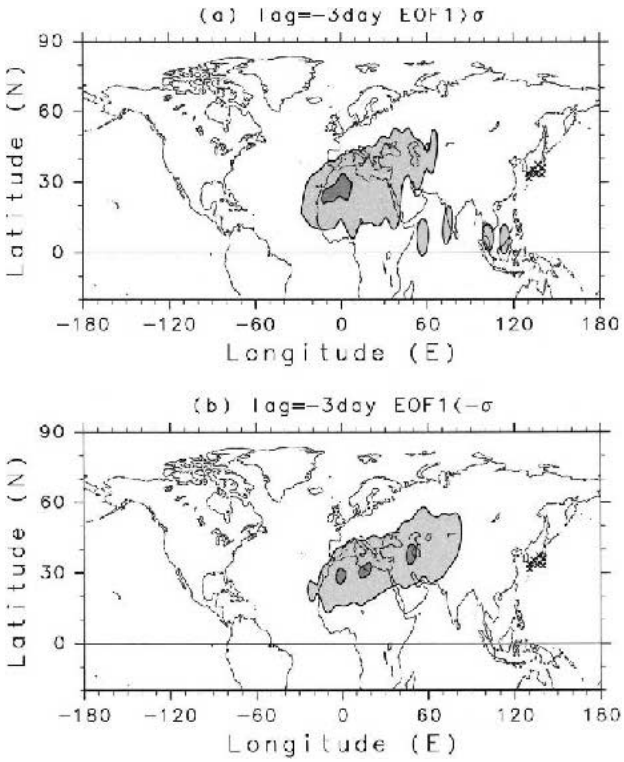

FIG. 21. The same as Fig. 19, but for EOF1.

where the disturbance amplitude is large (Fig. 12), $u'v'$ is negative. This feature is consistent with inertial instability.

It is worth noting that negative $u'v'$ eliminates the possibility that EOF2 disturbances are due to fluctuations of large-scale winds including the Hadley circulation, because the background wind is northeastward around EOF2 stations (see Fig. 14).

An interesting feature is that $u'v'$ values are positive to the north of the negative region. The meridional variation of $u'v'$ means that a deceleration of mean zonal wind occurs around 30°N where the subtropical jet axis is situated (Fig. 13). Also interesting is that the inertially unstable region extends to a relatively high latitude of 30°N. A numerical simulation by O'Sullivan and Hitchman (1992) showed similar extension of the unstable region to higher latitudes.

The growth rate of the inertially unstable mode for the zonally symmetric inviscid flow is maximized at infinitely small vertical wavelengths (Dunkerton 1981). However, for the case with finite eddy diffusivity, modes with smaller vertical wavelengths are stabilized. According to the Dunkerton (1981) theory, the marginal vertical wavenumber m_c (the vertical wavenumber of neutral viscous mode) is related to the eddy diffusivity ν:

$$m_c^5 = N\beta/4\nu^2. \quad (4)$$

By taking 3–5 km as the marginal vertical wavelength of observed layered disturbances, 10 min as a typical tropospheric value of the Brunt–Väisälä period, and a β value at the latitude 25°, the effective eddy diffusivity ν is estimated at 1.2–4.2 m^2 s^{-1}.

c. Inertia–gravity waves trapped in the westerly jet

As discussed in section 6a, there is little possibility of mountain waves with zero ground-based phase ve-

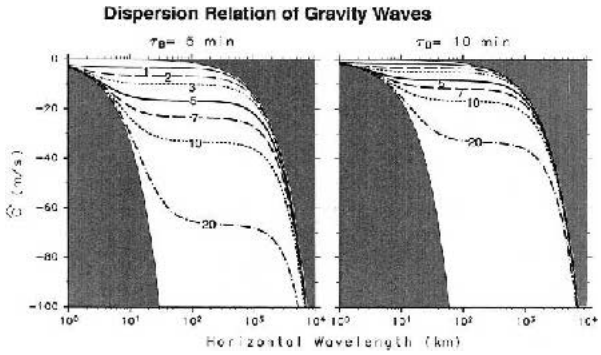

FIG. 22. Dispersion relation of inertia–gravity waves. The vertical axis shows the phase velocity (m s^{-1}) relative to the mean wind for buoyancy periods of (a) 5 min and (b) 10 min. Numerals on lines show vertical wavelength (km). Line types are taken to be the same for both figures to distinguish curves for different vertical wavelengths.

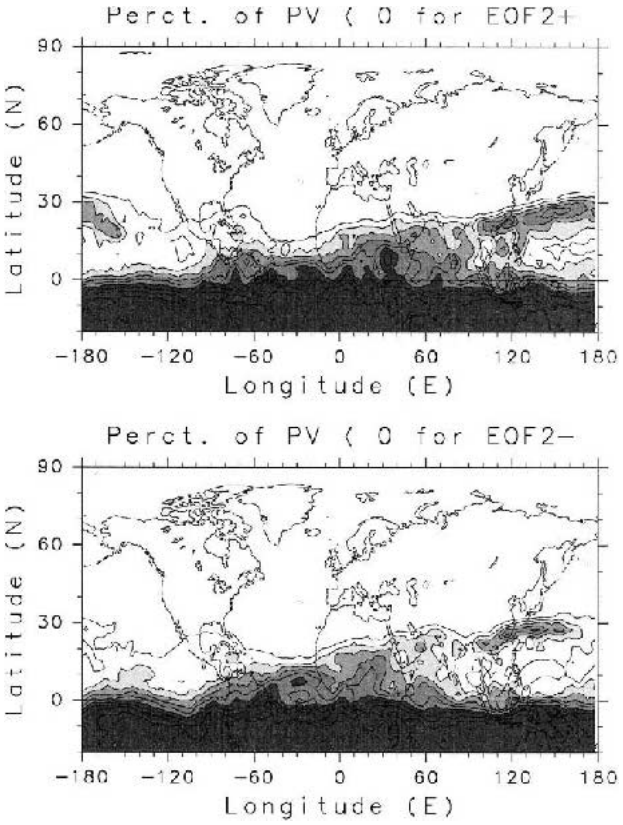

FIG. 23. The same as Fig. 15, but for (top) positive and (bottom) negative EOF2 cases.

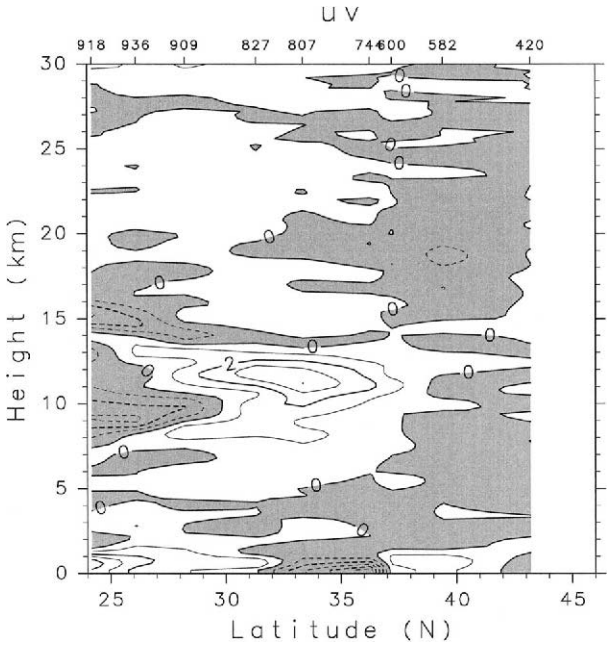

FIG. 24. Composite of $u'v'$ for positive EOF2 cases in the meridional cross section. Station locations indicated by numbers across top of figure.

locity. However, it is possible that the layered disturbances are due to inertia–gravity waves with nonzero ground-based phase velocities. It is seen from Fig. 22 that typical phase velocities relative to the mean wind for vertical wavelengths of 3–5 km are -5 to -20 m s^{-1}. If the wavevectors have large meridional components, the ground-based phase velocities can be very small and the ground-based wave periods can be long as observed. It is likely that EOF1 disturbances are due to such inertia–gravity waves. As mentioned in section 1, Hirota and Niki (1986) and Sato (1994) examined long lasting layered disturbances at Shigaraki near EOF1 stations by utilizing the MU radar data and showed that they are likely due to the inertia–gravity waves. In particular, Sato (1994) showed that inertia–gravity waves just above the westerly jet region propagate mostly meridionally. This is consistent with the above inference.

Such inertia–gravity waves hardly propagate outward from the core of the jet stream, as they encounter their critical levels (e.g., O'Sullivan and Dunkerton 1995). Thus, their energy should be confined to the jet core, consistent with the observation that EOF1 disturbances are dominant around the jet core (Fig. 12). This inertia–gravity wave guide may be leaky because the jet stream is not steady (Dunkerton 1984).

As stated above, EOF1 disturbances are not due to in situ inertial instability near Japan because PV is generally positive and takes stratospheric values around the disturbances. However, it is inferred that the generation of the disturbances may be related to inertial instability because the backward trajectories from a few southern EOF1 stations sometimes reach the equatorial region. Inertial instability is able to excite gravity waves with a restoring force of buoyancy because significant vertical motion is associated with an instability of finite latitudinal extent. Another candidate for gravity wave generation is spontaneous radiation from the jet itself (Fritts and Luo 1992; Luo and Fritts 1993; O'Sullivan and Dunkerton 1995).

An interesting and important feature is that u_{amp} is distributed in the $>$ shape for EOF1 disturbances in a meridional cross section (Fig. 12). This peculiar distribution is observed even in the climatological field of u_{amp} (Fig. 7). Sato (1994) showed by a statistical analysis using the MU radar in Japan (36°N, 135°E) that the meridional and vertical energy propagation of dominant inertia–gravity waves above the westerly jet in winter are equatorward and upward, respectively. The upper part of the $>$ shaped distribution is in harmony with her result.

7. Summary and concluding remarks

By analyzing operational Japanese radiosonde data archived with fine vertical resolution over 4 yr, it has been revealed that long-lived layered disturbances with strong meridional wind component appear in winter at

several stations simultaneously. They are dominant in the height range 8–16 km and in the latitude band within and slightly to the south of the midlatitude westerly jet. Results of an EOF analysis indicate that there are two dominant amplitude patterns of the disturbances. The first mode (EOF1) has large amplitude in the middle part of Japan (30°–37°N) while the second mode (EOF2) has large amplitude in the southern part of Japan (23°–30°N).

The background fields were examined using NCEP reanalysis data. It was found that EOF1 and EOF2 disturbances are most likely due to different phenomena, although the characteristics are similar in terms of their long duration, appearance at multiple stations, and short vertical scale. Results of back trajectory analysis showed that air parcels of EOF1 and EOF2 stations have different origins; this result was obtained independently of the EOF analysis.

EOF2 disturbances are likely due to inertial instability. Background potential vorticity is nearly zero and frequently negative. The air parcels where EOF2 disturbances are observed can be traced back to the equatorial region within a few days. The large amplitude of meridional wind component and negative covariance of zonal and meridional wind components are also consistent with unstable modes of inertial instability.

On the other hand, it is inferred that EOF1 disturbances are due to inertia–gravity waves trapped in the strong westerly jet. The long period of the disturbances can be explained by a significant Doppler shift by the mean wind. This inference is consistent with previous studies using an MST radar.

The backward trajectory analysis indicates that the south of Japan is the only location with high probability of negative potential vorticity at such relatively high latitudes. The climatological route of the anomalous PV is from far west and south of Japan. So, it will be interesting in future studies to examine the appearance of layered disturbances using data from operational or special observations at sites along this route.

An unresolved theoretical problem is why the disturbances persist over a long time. The timescale of layered disturbances may be determined by the timescale of anomalous air transport relative to that needed for neutralization.

Another important issue motivated by this study is that the inertial instability may generate gravity waves in the equatorial and subtropical regions. Parcels reaching the southernmost EOF1 stations are occasionally traced back to the equatorial region where PV values are anomalous, although the potential vorticity is positive and takes mostly stratospheric values by the time the air parcels reach EOF1 stations. The potential vorticity is modified by mixing processes associated with the inertial instability itself and by other processes. Such transmutation of air from a Lagrangian viewpoint should be addressed in future studies.

In the tropical region, vigorous convection is considered to be a dominant source of gravity waves. However, inertial instability may be an additional source. As indicated theoretically and observationally, the vertical scale of inertial instability is small compared with convective motions in the troposphere. Thus, inertial instability is able to excite gravity waves in a different spectral range from those of convective origin.

Acknowledgments. The authors thank Mr. Shoin Yagi in Meteorological Research Institute in Japan for kindly providing detailed information on the operational radiosonde observation archive at JMA. The GFD-DENNOU library was used for drawing figures. This research was supported in part by Grant-in-Aid for Scientific Research (B)(2) 12440126 of the Ministry of Education, Culture, Sports, Science and Technology in Japan, by the National Science Foundation Grant ATM-9903514, and by the National Aeronautics and Space Administration Contract NAS1-99130.

REFERENCES

Allen, S. J., and R. A. Vincent, 1995: Gravity wave activity in the lower atmosphere: Seasonal and latitudinal variations. *J. Geophys. Res.,* **100,** 1327–1350.

Ciesielski, P. E., D. E. Stevens, R. H. Johnson, and K. R. Dean, 1989: Observational evidence for asymmetric inertial instability. *J. Atmos. Sci.,* **46,** 817–831.

Clark, P. D., and P. H. Haynes, 1996: Inertial instability on an asymmetric low-latitude flow. *Quart. J. Roy. Meteor. Soc.,* **122,** 151–182.

Dunkerton, T. J., 1981: On the inertial stability of the equatorial middle atmosphere. *J. Atmos. Sci.,* **38,** 2354–2364.

——, 1983: A nonsymmetric equatorial inertial instability. *J. Atmos. Sci.,* **40,** 807–813.

——, 1984: Inertia–gravity waves in the stratosphere. *J. Atmos. Sci.,* **41,** 3396–3404.

——, 1993a: Inertial instability of nonparallel flow on an equatorial β plane. *J. Atmos. Sci.,* **50,** 2744–2758.

——, 1993b: Observation of 3–6-day meridional wind oscillations over the tropical Pacific, 1973–1992: Vertical structure and interannual variability. *J. Atmos. Sci.,* **50,** 3292–3307.

——, and M. P. Baldwin, 1995: Observation of 3–6-day meridional wind oscillations over the tropical Pacific, 1973–1992: Horizontal structure and propagation. *J. Atmos. Sci.,* **52,** 1585–1601.

Fritts, D. C., and Z. Luo, 1992: Gravity wave excitation by geostrophic adjustment of the jet stream. Part I: Two-dimensional forcing. *J. Atmos. Sci.,* **49,** 681–697.

Gill, A. E., 1982: *Atmosphere–Ocean Dynamics.* Academic Press, 662 pp.

Hayashi, H., M. Shiotani, and J. C. Gille, 1998: Vertically stacked temperature disturbances near the equatorial stratopause as seen in cryogenic limb array etalon spectrometer data. *J. Geophys. Res.,* **103,** 19 469–19 483.

Hirota, I., and T. Niki, 1986: Inertia–gravity waves in the stratosphere. *J. Meteor. Soc. Japan,* **64,** 995–999.

Hitchman, M. H., C. B. Leovy, J. C. Gille, and P. L. Bailey, 1987: Quasi-stationary zonally asymmetric circulations in the equatorial lower mesosphere. *J. Atmos. Sci.,* **44,** 3159–3176.

Japan Meteorological Agency, 1995: *Guideline for Aerological Observation.* Japan Meteorological Agency, 153 pp.

Kitamura, Y., and I. Hirota, 1989: Small-scale disturbances in the lower stratosphere revealed by daily rawinsonde observations. *J. Meteor. Soc. Japan,* **67,** 817–831.

Luo, Z., and D. C. Fritts, 1993: Gravity wave excitation by geo-

strophic adjustment of the jet stream. Part II: Three-dimensional forcing. *J. Atmos. Sci.*, **50,** 104–115.
O'Sullivan, D. J., and M. H. Hitchman, 1992: Inertial instability and Rossby wave breaking in a numerical model. *J. Atmos. Sci.*, **49,** 991–1002.
——, and T. J. Dunkerton, 1995: Generation of inertia–gravity waves in a simulated lifecycle of baroclinic instability. *J. Atmos. Sci.*, **52,** 3695–3716.
Sato, K., 1990: Vertical wind disturbances in the troposphere and lower stratosphere observed by the MU radar. *J. Atmos. Sci.*, **47,** 2803–2817.
——, 1994: A statistical study of the structure, saturation and sources of inertio-gravity waves in the lower stratosphere observed with the MU radar. *J. Atmos. Terr. Phys.*, **56,** 755–774.
——, H. Eito, and I. Hirota, 1993: Medium-scale traveling waves in the extratropical upper troposphere. *J. Meteor. Soc. Japan*, **71,** 427–436.
——, K. Yamada, and I. Hirota, 2000: Global characteristics of medium-scale tropopausal waves observed in ECMWF operational data. *Mon. Wea. Rev.*, **128,** 3808–3823.
Stevens, D. E., and P. Ciesielski, 1986: Inertial instability of horizontally sheared flow away from the equator. *J. Atmos. Sci.*, **43,** 2845–2856.
Tsuda, T., Y. Murayama, H. Wiryosumarto, S. W. B. Harijono, and S. Kato, 1994: Radiosonde observations of equatorial atmosphere dynamics over Indonesia. 1. Equatorial waves and diurnal tides. *J. Geophys. Res.*, **99,** 10 491–10 506.
Wada, K., T. Nitta, and K. Sato, 1999: Equatorial inertia–gravity waves in the lower stratosphere revealed by TOGA-COARE IOP data. *J. Meteor. Soc. Japan*, **77,** 721–736.
Yoshiki, M., and K. Sato, 2000: A statistical study of gravity waves in the polar regions based on operational radiosonde observation data. *J. Geophys. Res.*, **105,** 17 995–18 011.